



ELSEVIER

Finite Elements in Analysis and Design 28 (1997) 83–104

FINITE ELEMENTS
IN ANALYSIS
AND DESIGN

On the stability of mixed finite elements in large strain analysis of incompressible solids

Daniel Pantuso, Klaus-Jürgen Bathe*

Massachusetts Institute of Technology, Cambridge, MA 02139, USA

Abstract

Some mixed finite elements for large deformation analysis of incompressible solids are studied. The elements are based on the displacement/pressure and enhanced strain mixed formulations. Specifically, it is shown that a quadrilateral 4-node element that satisfies the inf-sup condition in linear analysis – and hence is an effective element in such conditions – fails in large strain analysis. The reasons for this element behavior are explored. Some comparisons of element predictive capabilities are given. © 1997 Elsevier Science B.V.

Keywords: Mixed finite elements; Loss of ellipticity; Large strains

1. Introduction

During the last years, many researchers have been working on the development of low-order two-dimensional and three-dimensional finite elements for the analysis of continuous media. Low-order finite elements can be particularly attractive because of their robustness and simplicity when compared to high-order elements, but effective low-order elements have been difficult to obtain. As is well known, the classical displacement-based formulation leads to inaccurate results in the analysis of incompressible media. Furthermore, shear locking behavior arises in bending dominated problems [1].

The shear locking behavior can be effectively avoided by using either assumed strain or assumed stress methods [1–3]. However, the incompressible situation represents a more complicated problem and several techniques have been developed to deal with the divergence free constraint,

*Corresponding author.

Let us consider an arbitrary hyperelastic material whose strain energy density function per unit of reference volume is denoted by \hat{W} . The total potential of the body with original volume 0V is

$$\Pi(\mathbf{u}, p) = \int_{^0V} \left\{ \hat{W}(\mathbf{C}) - \frac{1}{2\kappa} (\bar{p} - p)^2 \right\} d^0V + \Pi^{\text{EXT}} \quad (1)$$

where \mathbf{u} and p represent the displacement and pressure field, respectively, and \mathbf{C} denotes the Cauchy–Green deformation tensor. The quantity \bar{p} refers to the pressure obtained from the displacement field, the constant κ represents the bulk modulus of the material and Π^{EXT} denotes the potential due to the externally applied loads. The functional given in Eq. (1) is modified by enhancing the displacement gradient as follows:

$$\mathbf{H} = \text{Grad } \mathbf{u} + \tilde{\mathbf{H}}. \quad (2)$$

Accordingly, the deformation gradient \mathbf{X} and the deformation tensor \mathbf{C} are now given by

$$\mathbf{X} = \mathbf{I} + \text{Grad } \mathbf{u} + \tilde{\mathbf{H}}, \quad (3)$$

$$\mathbf{C} = (\mathbf{I} + \text{Grad } \mathbf{u} + \tilde{\mathbf{H}})^T (\mathbf{I} + \text{Grad } \mathbf{u} + \tilde{\mathbf{H}}). \quad (4)$$

Different enhancements in deformation measures have also been considered. For example, we could define the total deformation gradient as a multiplicative decomposition of two motions, one represented by the deformation gradient obtained from the displacement interpolation and the other obtained from the enhancement (see Ref. [13]).

The proper kinematic decomposition into spherical and deviatoric parts for large strain analysis is given using $\det \mathbf{X}$ and

$$\hat{\mathbf{X}} = (\det \mathbf{X})^{-1/3} \mathbf{X}, \quad (5)$$

$$\hat{\mathbf{C}} = (\det \mathbf{X})^{-2/3} \mathbf{X}^T \mathbf{X} = (\det \mathbf{X})^{-2/3} \mathbf{C}. \quad (6)$$

Substituting Eqs. (2)–(6) into Eq. (1) we have the following modified total potential:

$$\bar{\Pi}(\mathbf{u}, p, \tilde{\mathbf{H}}) = \int_{^0V} \left\{ \bar{W}(\hat{\mathbf{C}}, \det \mathbf{X}) - \frac{1}{2\kappa} (\bar{p} - p)^2 \right\} d^0V + \Pi^{\text{EXT}}. \quad (7)$$

Invoking stationarity of $\bar{\Pi}$ we obtain the governing variational equations of the problem,

$$D\bar{\Pi}[\delta \mathbf{u}] \equiv \int_{^0V} \left\{ D\bar{W}[\delta \mathbf{u}] - \frac{1}{\kappa} (\bar{p} - p) D\bar{p}[\delta \mathbf{u}] \right\} d^0V - \mathcal{R} = 0 \quad (8)$$

$$D\bar{\Pi}[\delta \tilde{\mathbf{H}}] \equiv \int_{^0V} \left\{ D\bar{W}[\delta \tilde{\mathbf{H}}] - \frac{1}{\kappa} (\bar{p} - p) D\bar{p}[\delta \tilde{\mathbf{H}}] \right\} d^0V = 0 \quad (9)$$

$$D\bar{\Pi}[\delta p] \equiv \int_{^0V} \frac{1}{\kappa} (\bar{p} - p) Dp[\delta p] d^0V = 0. \quad (10)$$

Here we have, for a generic variable θ ,

$$D\bar{\Pi}[\delta \theta] \equiv \frac{d}{d\varepsilon} \{ \bar{\Pi}(\theta + \varepsilon \delta \theta) \} |_{\varepsilon=0} \quad (11)$$

and

$$\mathcal{R} = -D\Pi^{\text{EXT}}[\delta\mathbf{u}]. \quad (12)$$

Eqs. (8)–(10) constitute a set of nonlinear variational equations. Introducing the finite element interpolations, a system of nonlinear algebraic equations is obtained. The Newton–Raphson method is employed to iteratively solve the resulting equations. While we use here the total Lagrangian formulation (referring the variables to the original configuration), the same finite element equations are also obtained using the updated Lagrangian formulation (in which we refer all variables to the current configuration), see [1].

2.2. Element interpolations

We use the standard four-node isoparametric interpolation for the original geometry and the total displacement field

$$\mathbf{x} = \sum_{i=1}^4 h_i(\mathbf{r})\mathbf{x}_i, \quad (13)$$

$$\mathbf{u} = \sum_{i=1}^4 h_i(\mathbf{r})\mathbf{u}_i. \quad (14)$$

In these equations, the h_i 's are the usual bilinear interpolation functions, \mathbf{r} indicates the isoparametric coordinates (r, s) , and \mathbf{x}_i and \mathbf{u}_i are the nodal point coordinates and nodal point displacements, respectively.

The enhancement in the deformation gradient is given by

$$\hat{\mathbf{H}} = \mathbf{G}(\mathbf{r})\boldsymbol{\alpha} \quad (15)$$

where $\hat{\mathbf{H}}$ contains the elements of $\tilde{\mathbf{H}}$

$$\hat{\mathbf{H}} = \begin{bmatrix} \tilde{H}_{11} \\ \tilde{H}_{22} \\ \tilde{H}_{12} \\ \tilde{H}_{21} \end{bmatrix}. \quad (16)$$

The components of the matrix $\mathbf{G}(\mathbf{r})$ in Eq. (15) are functions of the isoparametric coordinates. The vector $\boldsymbol{\alpha}$ contains the internal parameters that are condensed out at the element level prior to the assemblage process. The matrix $\mathbf{G}(\mathbf{r})$ has to satisfy the condition that its integral over the volume of the element must vanish. This condition does not assure a stable formulation but is necessary. Therefore, we must have that,

$$\int_{-1}^{+1} \int_{-1}^{+1} \mathbf{G}(\mathbf{r})J(\mathbf{r}) \, d\mathbf{r} = \mathbf{0} \quad (17)$$

where $J(\mathbf{r})$ is the Jacobian determinant for the transformation from the physical coordinates (x, y) to the isoparametric coordinates (r, s) .

For a regular quadrilateral element, $J(\mathbf{r})$ is constant and condition (17) will be satisfied as long as $\mathbf{G}(\mathbf{r})$ itself satisfies it. However, for a general distorted element the Jacobian determinant is not constant. The usual procedure is then to consider (15) and (17) in the isoparametric coordinate system with \mathbf{G}^* , $\hat{\mathbf{H}}^*$ and $\tilde{\mathbf{H}}^*$ instead of \mathbf{G} , $\hat{\mathbf{H}}$ and $\tilde{\mathbf{H}}$, respectively. A transformation to the actual coordinate system then gives

$$\tilde{\mathbf{H}}(\mathbf{r}) = \frac{J_0}{J(\mathbf{r})} \bar{\mathbf{X}}_0^{-T} \tilde{\mathbf{H}}^*(\mathbf{r}) \bar{\mathbf{X}}_0^{-1} \quad (18)$$

where

$$\bar{\mathbf{X}}_0 = \left. \frac{\partial \mathbf{x}(\mathbf{r})}{\partial \mathbf{r}} \right|_{\mathbf{r}=\mathbf{0}} \quad \text{and} \quad J_0 = J|_{\mathbf{r}=\mathbf{0}} \quad (19)$$

are the geometry gradient and its determinant evaluated at the center of the element.

We consider the plane strain case and define $\mathbf{G}^*(\mathbf{r})$ as (see [6])

$$\mathbf{G}^*(\mathbf{r}) = \begin{bmatrix} r & 0 & 0 & 0 & rs & 0 \\ 0 & s & 0 & 0 & 0 & rs \\ 0 & 0 & r & 0 & 0 & 0 \\ 0 & 0 & 0 & s & 0 & 0 \end{bmatrix}. \quad (20)$$

According to expressions (15) and (20) the enhanced part of the displacement gradient is obtained as

$$\hat{\mathbf{H}}^*(\mathbf{r}) = \begin{bmatrix} r\alpha_1 + rs\alpha_5 \\ s\alpha_2 + rs\alpha_6 \\ r\alpha_3 \\ s\alpha_4 \end{bmatrix} \quad (21)$$

or written in matrix form,

$$\tilde{\mathbf{H}}^*(\mathbf{r}) = \begin{bmatrix} r\alpha_1 + rs\alpha_5 & r\alpha_3 \\ s\alpha_4 & s\alpha_2 + rs\alpha_6 \end{bmatrix}. \quad (22)$$

The pressure interpolation is obtained using the same interpolation functions as used for the displacements and geometry. Namely we have,

$$p = \sum_{i=1}^4 h_i(\mathbf{r}) p_i \quad (23)$$

where the p_i 's are the nodal point pressure values. Hence the element yields a continuous pressure field across the element boundaries.

We wish to remark that this seems to be the only possible option of pressure interpolation if the inf-sup condition is to be satisfied. Namely, considering the linear analysis case and a square element of side length 2, the volumetric strain due to the displacements and the enhancement in the

strain components is given by

$$\varepsilon_v = \mathbf{B}_v \mathbf{U} + \mathbf{G}_v \boldsymbol{\alpha} \quad (24)$$

where

$$\mathbf{B}_v = \frac{1}{4} [(1+s)(1+r) - (1+s)(1-r) - (1-s) - (1-r)(1-s) - (1+r)] \quad (25)$$

$$\mathbf{G}_v = [r \ s \ 0 \ 0 \ rs \ rs]. \quad (26)$$

Let us first consider the case of a discontinuous pressure field across the element boundaries, and consider the constant pressure term in the field. Recall that we have a spurious pressure mode p_s if [1]

$$\int_V p_s \varepsilon_{v_h} dV = 0 \quad \forall \varepsilon_{v_h} \in \Xi_h^{\text{vol}} \quad (27)$$

where Ξ_h^{vol} is the space of volumetric strains reached by the nodal point displacements and the strain enhancement modes given in Eq. (24), and ε_{v_h} is an element in that space.

As is well-known, the 4/1 (or Q1/P0) element, with the volumetric strain displacement interpolation of Eq. (25), contains the spurious pressure mode shown in Fig. 2(a) (see for example Ref. [1]), and clearly each of the volumetric strain terms in Eq. (26) also integrates to zero over the element volume. Hence, Eq. (27) is satisfied and the mode in Fig. 2(a) is also a spurious pressure mode for such an element. Therefore, the pressure has to be continuous and the linear pressure distribution is the natural one to use.

Let us also note that if we discard the last two columns in \mathbf{G}^* and consider the linear continuous pressure field, the pressure distribution depicted in Fig. 2(b) is a spurious pressure mode. The proof is as follows. The pressure inside each element is given by

$$p = \gamma_1 + \gamma_2 r + \gamma_3 s + \gamma_4 rs. \quad (28)$$

Now we need to evaluate over each element (m) the integral

$$\int_{V^{(m)}} (\gamma_1 + \gamma_2 r + \gamma_3 s + \gamma_4 rs) [\mathbf{B}_v \mathbf{U} + \mathbf{G}_v \boldsymbol{\alpha}] dV^{(m)} \quad (29)$$

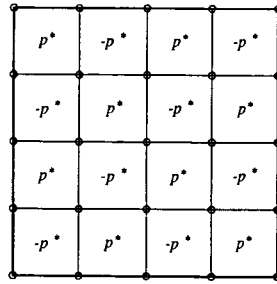
and we have with Eqs. (24)–(26), for element (m),

$$\int_{V^{(m)}} \gamma_1 [\mathbf{B}_v \mathbf{U} + \mathbf{G}_v \boldsymbol{\alpha}] dV^{(m)} = \gamma_1 [u_1 + v_1 - u_2 + v_2 - u_3 - v_3 + u_4 - v_4], \quad (30)$$

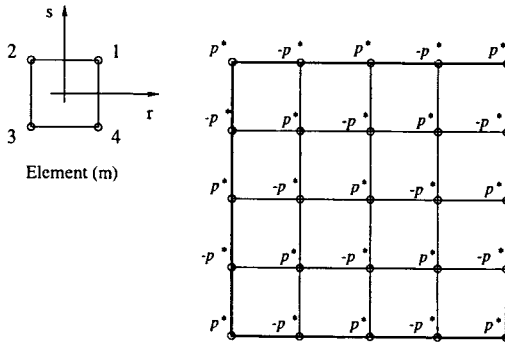
$$\int_{V^{(m)}} \gamma_2 r [\mathbf{B}_v \mathbf{U} + \mathbf{G}_v \boldsymbol{\alpha}] dV^{(m)} = \frac{\gamma_2}{4} [v_1 - v_2 + v_3 - v_4 + 4\alpha_1] \int_{V^{(m)}} r^2 dV^{(m)}, \quad (31)$$

$$\int_{V^{(m)}} \gamma_3 s [\mathbf{B}_v \mathbf{U} + \mathbf{G}_v \boldsymbol{\alpha}] dV^{(m)} = \frac{\gamma_3}{4} [u_1 - u_2 + u_3 - u_4 + 4\alpha_2] \int_{V^{(m)}} s^2 dV^{(m)}, \quad (32)$$

$$\int_{V^{(m)}} \gamma_4 rs [\mathbf{B}_v \mathbf{U} + \mathbf{G}_v \boldsymbol{\alpha}] dV^{(m)} = \gamma_4 [\alpha_5 + \alpha_6] \int_{V^{(m)}} r^2 s^2 dV^{(m)}. \quad (33)$$



(a) Checkerboard pressure distribution in assemblage of square 4/1 elements.
Discontinuous pressure



(b) Checkerboard pressure distribution in assemblage of square 4/4-c/4 elements.
Continuous pressure

Fig. 2. Spurious pressure modes for element assemblages. The displacements are fixed everywhere on the boundary.

Note that if the last two columns of \mathbf{G}^* are not included, then the integral considered in Eq. (33) is automatically zero. However, for the pressure distribution depicted in Fig. 2(b) only the γ_4 associated pressure term is present, that is, for each element

$$p^{(m)} = p^* rs \operatorname{sgn}(p_1^{*(m)}) \quad (34)$$

where $p_1^{*(m)}$ is the nodal value of the pressure at the local node 1 of element (m) , see Fig. 2(b). The evaluation of (27) for the element assemblage then gives

$$\int_V p \varepsilon_{v_n} dV = \sum_m p^* \operatorname{sgn}(p_1^{*(m)}) \left\{ \int_{V^{(m)}} (rs) \varepsilon_{v_n} dV^{(m)} \right\} = 0 \quad \forall \varepsilon_{v_n} \in \Xi_h^{\text{vol}} \quad (35)$$

and therefore the pressure distribution depicted in Fig. 2(b) is a spurious pressure mode.

The contribution of α_5 and α_6 to the integral defined in Eq. (33) assures that there exists no spurious pressure mode when $\mathbf{G}^*(\mathbf{r})$ as defined in Eq. (20) is employed.

3. The hour-glass mode and stability

The appearance of the hour-glass mode is associated with a nonphysical loss of stability of the problem under consideration. Namely, there is a negative eigenvalue that becomes very large in absolute value and the corresponding eigenvector dominates the deformations.

3.1. Eigensolution of a compression test

To gain insight into the appearance of the hour-glass mode, we analyze a simple compression test. The model is depicted in Fig. 3. A rubber-like material of the Mooney-Rivlin type is considered [1],

$$\bar{W} = C_1(J_1 - 3) + C_2(J_2 - 3) + \frac{\kappa}{2}(J_3 - 1)^2 \quad (36)$$

where the J_i are the reduced invariants of the deformation gradient,

$$J_1 = I_1 I_3^{-1/3}, \quad (37)$$

$$J_2 = I_2 I_3^{-2/3}, \quad (38)$$

$$J_3 = I_3^{1/2} = \det X \quad (39)$$

and the I_i are the invariants of the Cauchy–Green deformation tensor. We used in our analysis $C_1 = 2.0$, $C_2 = 0.2$ and $\kappa = 1.0 \times 10^3$, so that we have an almost incompressible material. The

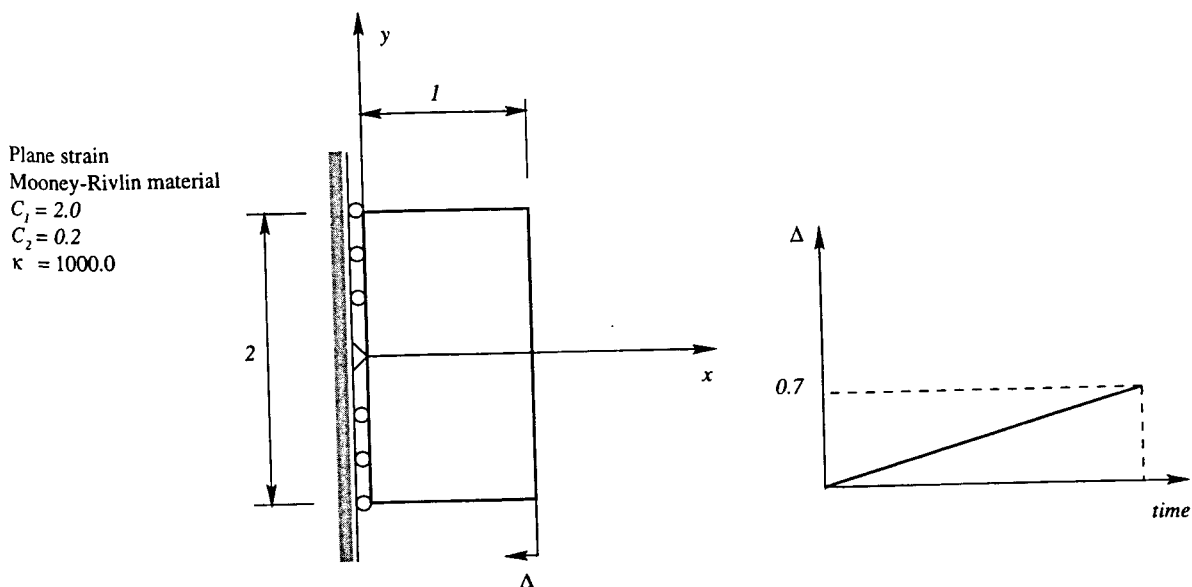


Fig. 3. Compression test. The displacement Δ is imposed very slowly, hence a static analysis is performed.

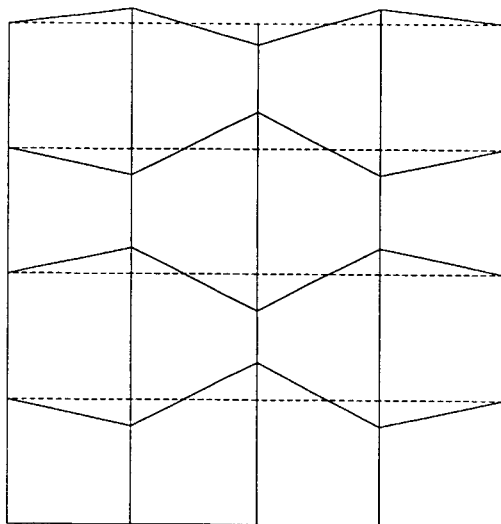


Fig. 4. Hour-glass pattern for the 4×4 mesh, discretizing half the specimen, and using the 4/4-c/6 element.

analysis is accomplished as follows: we consider 4×4 , 8×8 and 16×16 meshes for half the specimen, using symmetry conditions, gradually (that is neglecting inertia effects) increase the prescribed displacement Δ from 0 to 0.7, and study the eigenvalues and corresponding eigenvectors of the stiffness matrix obtained for the complete finite element discretization as a function of the imposed deformation. In the case of the 4/4-c/6 element discretizations, we first condensed out the pressure degrees of freedom and then performed the eigenanalysis. Hence, the following problem is solved for each load step,

$${}^t_0\mathbf{K}\phi_i = \lambda_i\phi_i; \quad i = 1, 2, \dots \quad (40)$$

where ${}^t_0\mathbf{K}$ represents the stiffness matrix calculated at the beginning of the step considered and referred to the original configuration, λ_i is an eigenvalue and ϕ_i is the corresponding eigenvector.

We performed the analysis using the 4/4-c/6 element and also the displacement/pressure 9/3 element [1]. Figs. 4 and 5 show typical hour-glass patterns obtained using the 4/4-c/6 element for the 4×4 and the 8×8 meshes, respectively. The original meshes are also shown with dashed lines in both figures.

It is expected that, due to the strong compression, loss of stability takes place at some level of deformation and, as a consequence, negative eigenvalues will appear. We give in Table 1 the number of negative eigenvalues calculated as a function of the imposed displacement Δ . Notice that, even though the 9/3 element discretization has more degrees of freedom than the corresponding model using the 4/4-c/6 element, it contains a fewer number of negative eigenvalues. This indicates that non-physical modes arise as the applied displacement increases when using the 4/4-c/6 element discretization.

We monitored the smallest eigenvalue (or largest negative eigenvalue) as a function of the applied displacement Δ . The results are plotted in Figs. 6 and 7 for the 4×4 and 8×8 meshes.

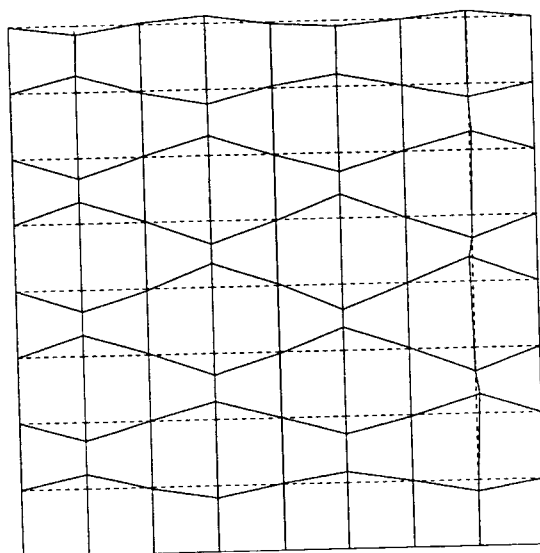


Fig. 5. Hour-glass pattern for the 8×8 mesh, discretizing half the specimen, and using the 4/4-c/6 element.

Table 1
Number of negative eigenvalues as a function of the imposed displacement Δ

Δ	9/3 element			4/4-c/6 element		
	4 \times 4	8 \times 8	16 \times 16	4 \times 4	8 \times 8	16 \times 16
0.0	0	0	0	0	0	0
0.1	0	0	0	0	0	0
0.2	0	0	0	0	0	0
0.3	0	0	0	5	25	101
0.4	2	3	6	7	25	99
0.5	4	8	16	5	23	93
0.6	4	8	16	5	23	96
0.7	4	8	16	6	26	104

respectively. We should note the difference between the results obtained with the 4/4-c/6 and the 9/3 elements. Considering the 4/4-c/6 element discretizations, in each case the smallest eigenvalue decreases very rapidly to a large negative number. The corresponding eigenvector represents an hour-glass mode. There are also other modes that correspond to hour-glassing and whose eigenvalues are also very large in negative values. The remaining negative eigenvalues (which do not correspond to hour-glass modes) stay of the same order of magnitude throughout the analysis and are much smaller in absolute values. Clearly, the very large negative eigenvalues lead to the appearance of the hour-glass modes in an incremental analysis. In contrast, the 9/3 element discretizations give reasonable negative eigenvalues throughout the analysis and none of them

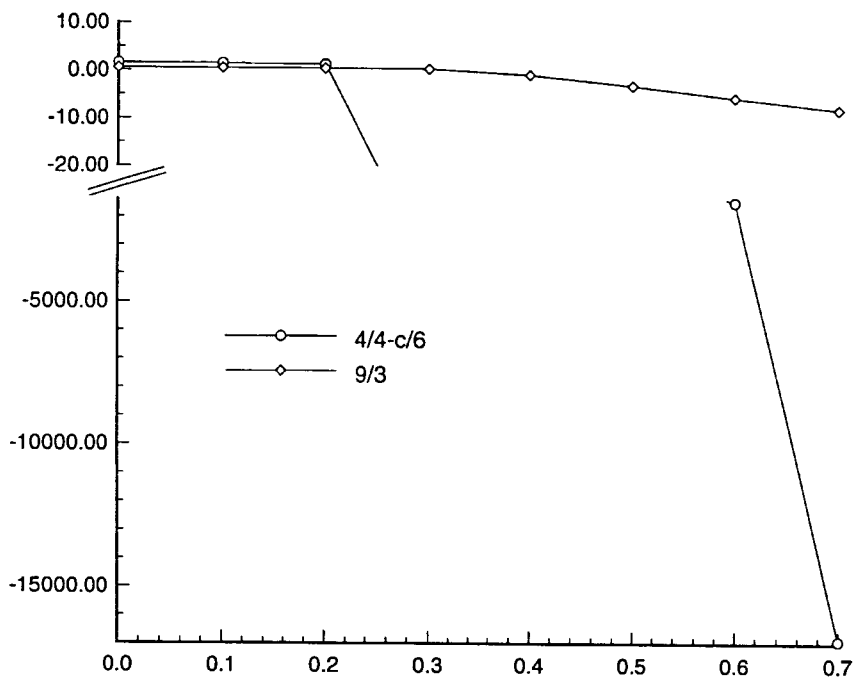


Fig. 6. Smallest eigenvalue as a function of the imposed displacement Δ for the 4×4 mesh discretization.

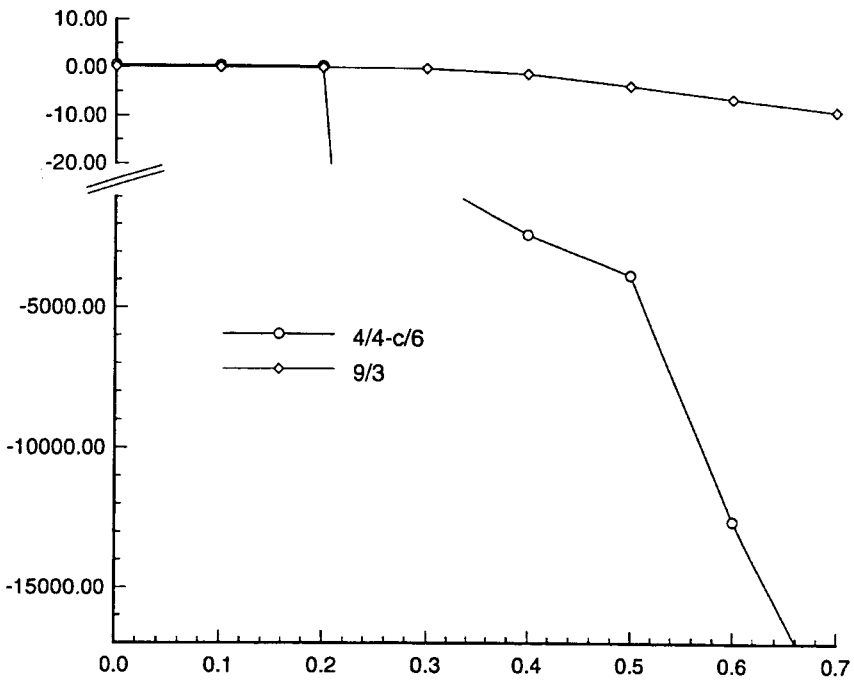


Fig. 7. Smallest eigenvalue as a function of the imposed displacement Δ for the 8×8 mesh discretization.

correspond to an hour-glass mode. Hence, hour-glassing is not expected when using the 9/3 element.

3.2. The inf-sup and ellipticity conditions

The following question arises in general: “Why is it that even though the 4/4-c/6 element satisfies the inf-sup condition (in linear analysis), the discretizations still fail in large strain analysis due to the appearance of the hour-glass mode?”. To answer this question we need to investigate whether the ellipticity and inf-sup conditions are satisfied in large deformation analysis.

Let us consider a typical current configuration of the body in the incremental solution. Let Vol be the volume of the body and let us introduce the following spaces:

$$\Xi = \Xi^c \oplus \Xi^e, \quad (41)$$

$$\Xi^c = \nabla(V), \quad (42)$$

$$V = \{v/v_i, \partial_{x_j} v_i \in L^2(Vol), i, j = 1, 2, 3\}, \quad (43)$$

$$\Xi^e = \left\{ \tilde{\xi}/\tilde{\xi}_{ij} \in L^2(Vol) \text{ and } \int_{Vol} \tilde{\xi}_{ij} dVol = 0, i, j = 1, 2, 3 \right\}, \quad (44)$$

$$Q = \{q/q \in L^2(Vol)\}. \quad (45)$$

Hence, we have that the space Ξ is split into the direct sum of Ξ^c and Ξ^e . The space Ξ^c is the space of gradients of functions in V whereas the space Ξ^e is the strain enhancement space. Note that it is possible to define a continuous operator G such that

$$G: \Xi^e \rightarrow V$$

$$\xi^e \rightarrow v \text{ with } v \text{ such that } \nabla(v) = \xi^e \quad (46)$$

with $\xi^e \in \Xi^e$.

The space $L^2(Vol)$ denotes the space of square integrable functions in Vol . Assuming that zero displacements are prescribed on the boundary S_u of the body, we also define the space V_0 as,

$$V_0 = \{v/v_i, \partial_{x_j} v_i \in L^2(Vol), i, j = 1, 2, 3; v_i|_{S_u} = 0, i = 1, 2, 3\}. \quad (47)$$

Hence, we also have the space Ξ_0 which is defined as $\Xi_0 = \Xi_0^c \oplus \Xi^e$ and $\Xi_0^c = \nabla(V_0)$. We assume that the prescribed displacements, at a minimum, do not allow rigid body motions.

The discrete finite element spaces are denoted by Ξ_{0h} and Q_h , and correspond to the interpolation functions presented in Section 2.2. They are subspaces of Ξ_0 and Q , respectively. Note that the spaces Ξ_{0h}^c and Ξ_{0h} correspond to strain spaces and the compatibility conditions must be satisfied when choosing the finite element interpolations. In our case, we use linear functions and, therefore, these conditions are automatically satisfied.

A typical Newton–Raphson iteration step for the solution of Eqs. (8)–(10), after condensing out the degrees of freedom corresponding to Eq. (9), can now be written as:

Find $\varepsilon_h \in \Xi_{0_h}$ and $p_h \in Q_h$ such that

$$a(\varepsilon_h, \xi_h) + b(\xi_h, p_h) = \langle f, G_h(\xi_h^c) \rangle \quad \forall \xi_h \in \Xi_{0_h}, \quad (48)$$

$$b(\varepsilon_h, q_h) - c(p_h, q_h) = \langle g, q_h \rangle \quad \forall q_h \in Q_h. \quad (49)$$

Here, $a(\cdot, \cdot)$ is the bilinear form of the elasticity problem considered, see [1], the forms, $b(\cdot, \cdot)$ and $c(\cdot, \cdot)$ correspond to the (almost) incompressibility constraint, and the right-hand sides in Eqs. (48) and (49) are due to the residuals in force balance, f , and constraint, g .

The two mathematical conditions for existence, uniqueness, stability and optimality of the solution of (48)–(49) are the ellipticity and inf-sup conditions [1, 4, 14], which we consider for the case of total incompressibility.

The ellipticity condition is,

$$a(\xi_h, \xi_h) \geq \beta_1 \|\xi_h\|^2 \quad \forall \xi_h \in K_h \quad (50)$$

where β_1 is a constant independent of h and greater than zero, and

$$K_h = \{\xi_h \in \Xi_{0_h} \text{ such that } \xi_{v_h} = 0\} \quad (51)$$

where ξ_{v_h} denotes the volumetric strain in Ξ_{0_h} . Once the ellipticity condition is satisfied, the *inf-sup condition*,

$$\inf_{q_h \in Q_h} \sup_{\xi_h \in \Xi_{0_h}} \frac{b(q_h, \xi_h)}{\|q_h\|_{Q_h} \|\xi_h\|_{\Xi_{0_h}}} \geq \beta_2 > 0 \quad (52)$$

where β_2 is a constant independent of h , is the criterion for stability and optimality of the solution.

In our incremental finite element solution we clearly do not satisfy – from a particular deformation level onward – the ellipticity condition and hence, we have strictly lost the mathematical stability of the solution. While the small negative eigenvalues (as encountered in the 9/3 element discretizations) nevertheless allow a physically realistic solution, the large negative eigenvalues (as encountered in the 4/4-c/6 element discretizations) lead to the non-physical hour-glassing. We note also that the space K_h is larger in the discretizations using the 9/1 element (assuming a constant pressure in the 9-node element, see Fig. 1) than using the 9/3 element. Hence, the loss of ellipticity (that is, the violation of (50)) must be expected “to occur more easily” when using the 9/1 element. And indeed, we will observe in the next section that an hour-glass mode does appear when using the 9/1 element in an analysis case in which the 9/3 element discretization does not show such mode.

4. Numerical tests

We consider in this section two problems in which the hour-glass mode appears: a plate with a hole subjected to tension and compression conditions and a rubber bushing in compression. The plate analysis does not show an hour-glass mode when tension conditions are considered. However, under a compressive load, the hour-glass mode appears. In the rubber bushing problem the hour-glass mode appears already at very early stages of deformation.

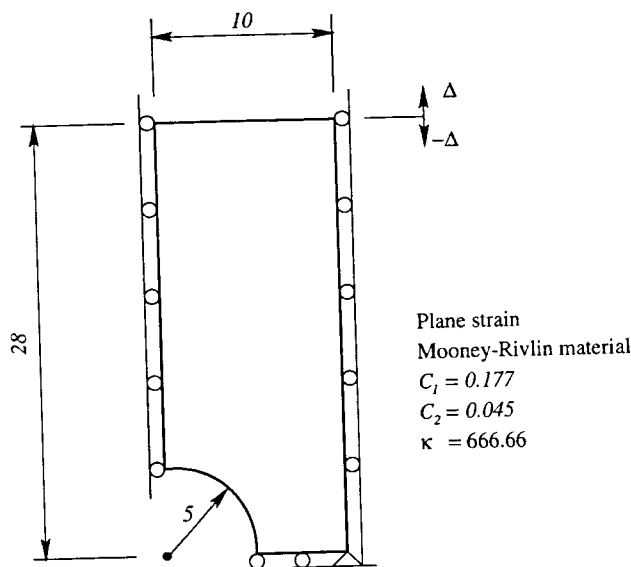


Fig. 8. Plate with a hole. Model problem.

The constitutive law used in these two cases is that given by Eq. (36) with the following values for the constants:

$$C_1 = 0.177, \quad (53)$$

$$C_2 = 0.045, \quad (54)$$

$$\kappa = 666.66. \quad (55)$$

4.1. Plate with a hole

This is a classical problem widely used as a numerical test in finite element analysis. The model problem is depicted in Fig. 8. We have considered both, a downward and an upward vertical displacement imposed at the top of the specimen.

The deformed configurations for a vertical displacement corresponding to two different values of Δ are shown in Figs. 9–11. The deformed configurations of the 4/4-c/6 and the 9/1 element discretizations show the hour-glass pattern. Note that using the 4/4-c/6 element the pattern extends throughout the mesh while using the 9/1 element the hour-glass mode is localized to near the hole. Convergence was harder to achieve for the 4/4-c/6 and 9/1 element discretizations at larger deformations and it was not possible to obtain the solution for the imposed displacement of $\Delta = -1.0$.

The force–displacement curves displayed in Fig. 12 show good correspondence between the results obtained with the 9/3 and the 4/4-c/6 element until the hour-glass mode appears in the 4/4-c/6 element model.

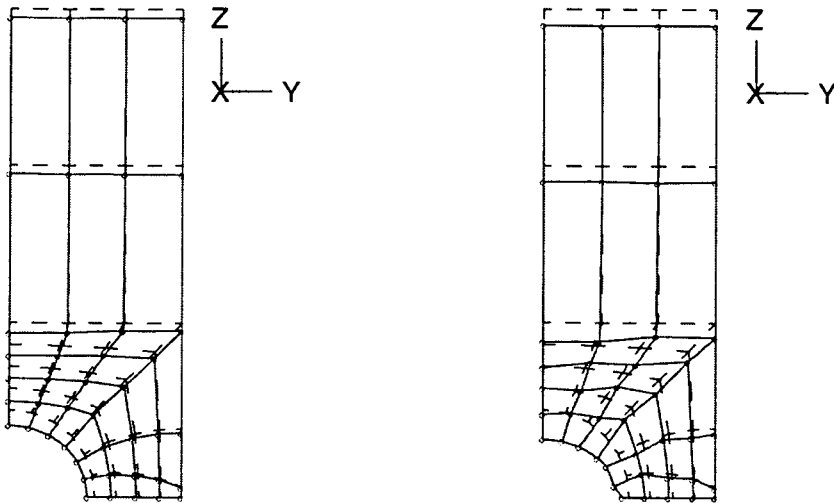


Fig. 9. Plate with a hole. Deformed configurations corresponding to vertical displacements of $\Delta = -0.5$ and $\Delta = -0.930$ using the 4/4-c/6 element.

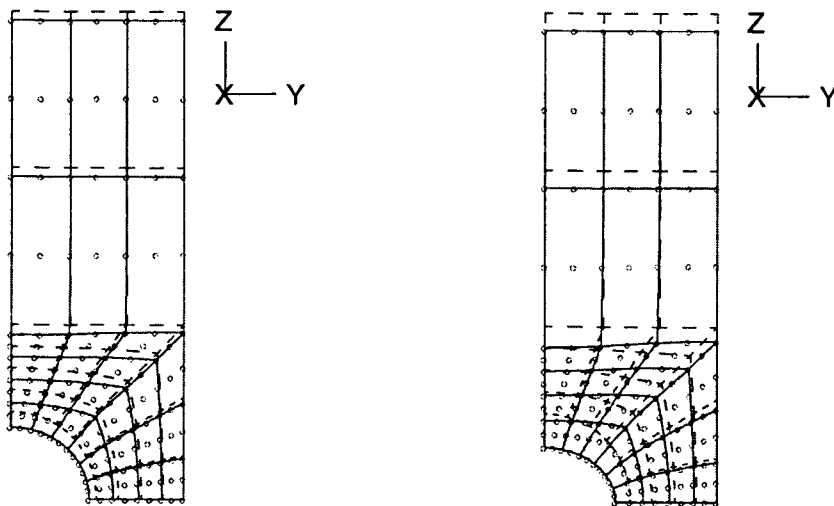


Fig. 10. Plate with a hole. Deformed configurations corresponding to vertical displacements of $\Delta = -0.5$ and $\Delta = -1.0$ using the 9/3 element.

The results when the plate is subjected to tension are shown in Fig. 13 only for the 4/4-c/6 element discretization. As seen, the hour-glass mode did not appear in this case.

4.2. Rubber bushing

Fig. 14 shows the cross section of the rubber bushing. We assume that the frame and internal shaft are rigid and that the rubber is perfectly bonded to these components. This example was also

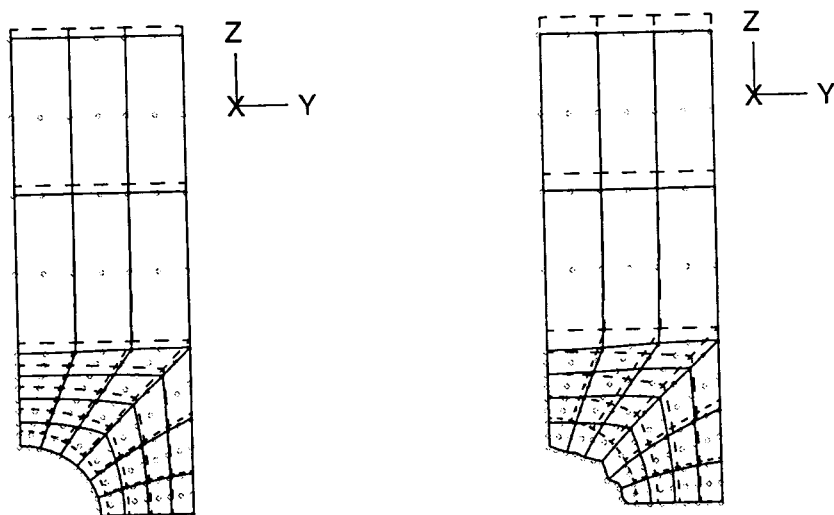


Fig. 11. Plate with a hole. Deformed configurations corresponding to vertical displacements of $\Delta = -0.5$ and $\Delta = -0.946$ using the 9/1 element.

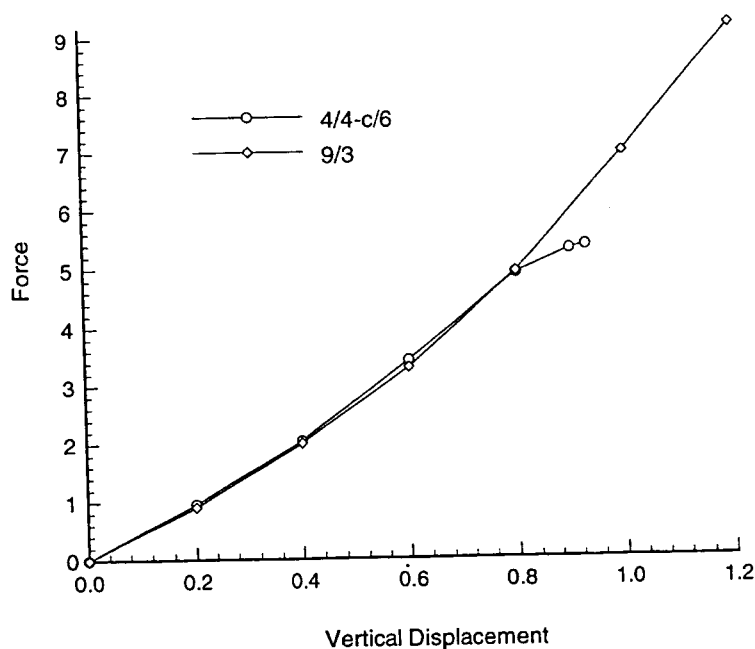


Fig. 12. Plate with a hole. Force–displacement curve.

considered in Ref. [12]. In this problem the hour-glass mode appears at very early stages of deformation.

The models considered consisted of 32 elements when we used the 4/4-c/6 and 9/3 elements, and 32 and 128 elements when we employed the 4/1 element.

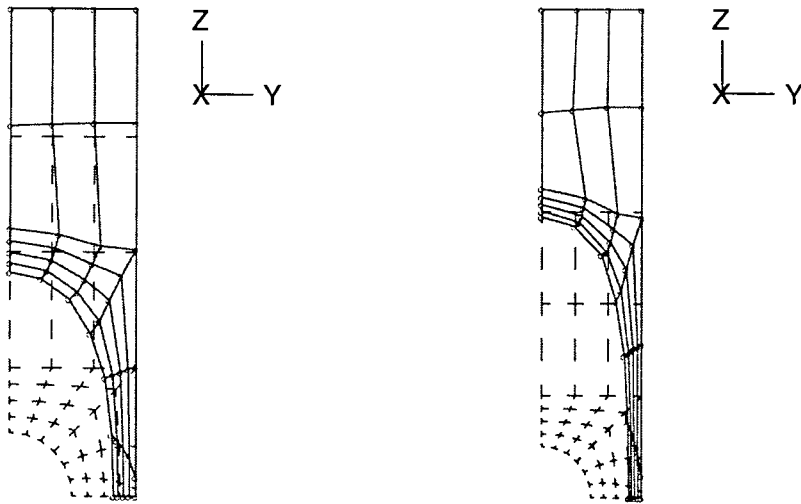


Fig. 13. Plate with a hole. Deformed configurations corresponding to vertical displacements of $\Delta = 5.0$ and $\Delta = 10.0$ using the 4/4-c/6 element.

Plane strain
Mooney-Rivlin material
 $C_1 = 0.177$
 $C_2 = 0.045$
 $\kappa = 666.66$

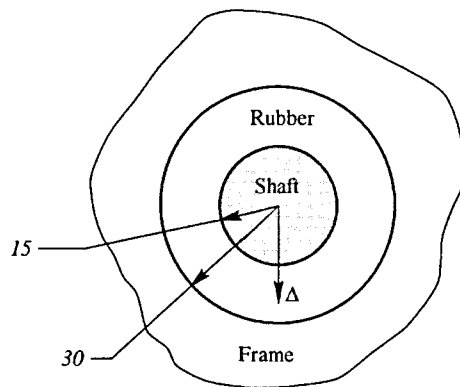


Fig. 14. Rubber bushing. Model problem.

Figs. 15–18 show the deformed configurations of the different models. The hour-glass mode appears for the model based on the assumed displacement gradient approach whereas it does not appear for the 4/1 and the 9/3 element discretizations. The hour-glass mode appeared when the applied displacement was approximately $\Delta = 2.3$. In contrast, no negative pivots were found during the factorizations of the stiffness matrices throughout the solutions using the 4/1 and the 9/3 elements.

Regarding the convergence in the iterations, both, the 9/3 and the 4/1 element discretizations reached a displacement of $\Delta = 8$ in eight equal load steps. It was not possible to achieve this level of deformation with the enhanced displacement gradient approach. In fact, convergence was harder

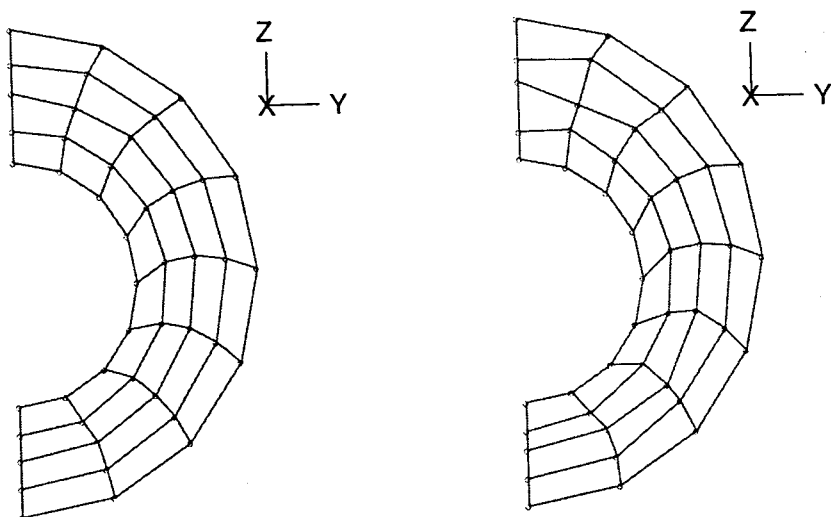


Fig. 15. Rubber bushing. Deformed configurations using the 4/4-c/6 element.

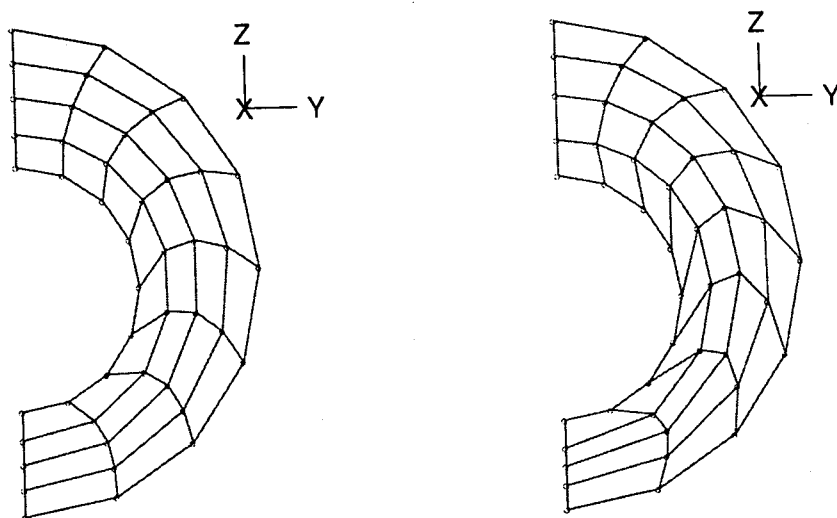


Fig. 16. Rubber bushing. Deformed configurations using 32 4/1 elements.

and almost impossible to achieve after the hour-glass mode appeared and tiny load steps had to be imposed to continue the analysis.

The force-deflection curves given in Fig. 19 show that, as expected, using the 4/1 element, the 32 element discretization is very much stiffer than the 9/3 element model of the problem, but using the finer 4/1 element model a better correspondence between the 4/1 and 9/3 element results is achieved.

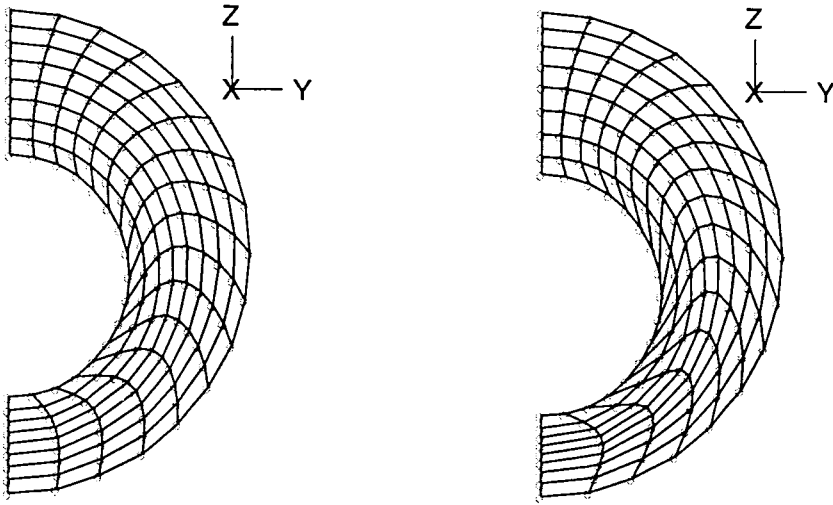


Fig. 17. Rubber bushing. Deformed configurations using 128 4/1 elements.

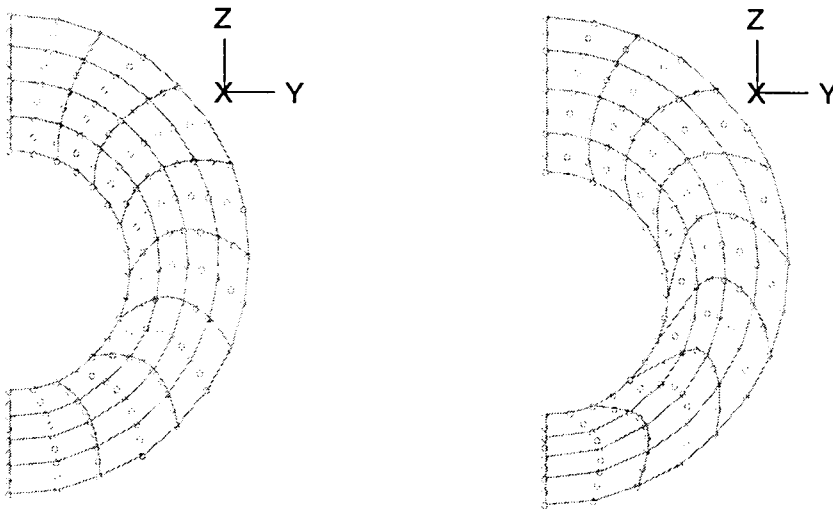


Fig. 18. Rubber bushing. Deformed configurations using the 9/3 element.

5. Conclusions

Our study, reported in this paper, regarding the performance of finite elements in the analysis of (almost) incompressible large strain response leads to some important conclusions.

Only elements that satisfy the inf-sup condition in linear analysis should be used. However, even such elements may not perform well in large strain solutions. The 4-node element proposed in [6] for linear analysis is such an element. In large strain solutions, an hour-glass mode can develop.

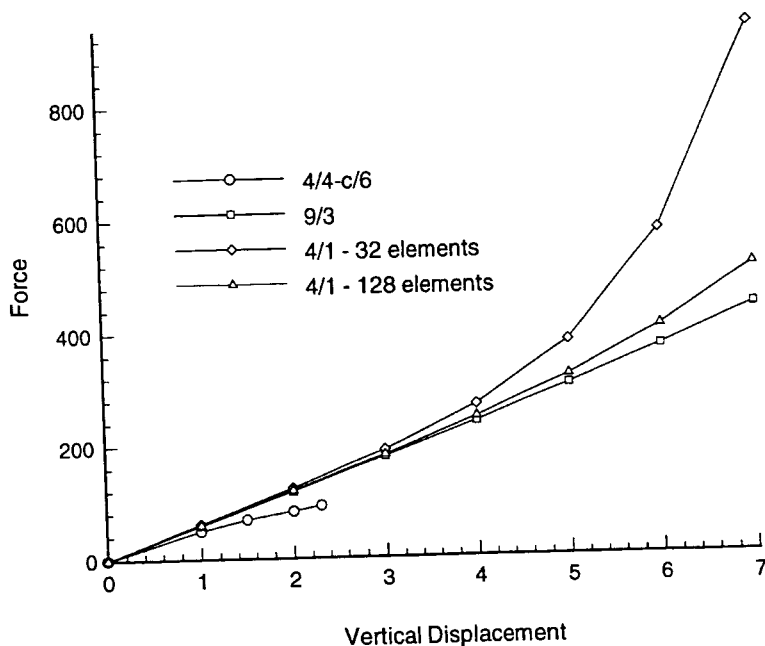


Fig. 19. Rubber bushing. Force-displacement curve.

This mode corresponds to a very large negative eigenvalue. As the mesh is refined, more such excessively large and nonphysical negative eigenvalues appear.

The most effective element for two-dimensional large strain analysis appears to be the 9/3 displacement/pressure element. For three-dimensional solutions its counterpart is the 27/4 element [1].

In this paper we concentrated upon exposing the basic difficulties encountered. A detailed mathematical analysis of the occurrence of the hour-glass mode would be very valuable.

Acknowledgement

We are grateful for the support provided by the Rocca fellowship for D. Pantuso's studies at MIT.

References

- [1] K.J. Bathe, *Finite Element Procedures*, Prentice Hall, Englewood Cliffs, NJ, 1996.
- [2] E.N. Dvorkin, S.I. Vasolo, A quadrilateral 2d finite element based on mixed interpolation of tensorial components, *Eng. Comput.* 6 (1989) 217–224.
- [3] T.H.H. Pian, K. Sumihara, Rational approach for assumed stress finite elements, *Int. J. Num. Methods Eng.* 20 (1984) 1685–1695.

- [4] F. Brezzi, M. Fortin. *Mixed and Hybrid Finite Element Methods*, Springer, Berlin, 1991.
- [5] J.C. Simo, M.S. Rifai, A class of mixed assumed strain methods and the method of incompatible modes, *Int. J. Numer. Methods Eng.* 29 (1990) 1595–1638.
- [6] D. Pantuso, K.J. Bathe, A four-node quadrilateral mixed-interpolated element for solids and fluids, *Math. Models Methods Appl. Sci.* 5 (1995) 1113–1128.
- [7] C. Lovadina, Analysis of strain-pressure finite element methods for the Stokes problem, to be published.
- [8] T. Belytschko, L.P. Bindeman, Assumed strain stabilization of the 4-node quadrilateral with 1-point quadrature for nonlinear analysis, *Comput. Methods Appl. Mech. Eng.* 88 (1991) 311–340.
- [9] E.A. De Souza Neto, D. Perić, G.C. Huang, D.R.J. Owen, Remarks on the stability of enhanced strain elements in finite elasticity and elastoplasticity, *Commun. Numer. Methods Eng.* 11 (1995) 951–961.
- [10] P. Wriggers, S. Reese, A note on enhanced strain methods for large deformations, *Comput. Methods Appl. Mech. Eng.* 135 (1996) 201–209.
- [11] M.A. Crisfield, G.F. Moita, G. Jelenić, L.P.R. Lyons, Enhanced lower-order element formulations for large strains, *Comput. Mech.* 17 (1–2) (1995) 62–73.
- [12] T. Sussman, K.J. Bathe, A finite element formulation for nonlinear incompressible elastic and inelastic analysis, *Comput. Struct.* 26 (1987) 357–409.
- [13] J.C. Simo, F. Armero, Geometrically non-linear enhanced strain mixed methods and the method of incompatible modes, *Int. J. Numer. Methods Eng.* 33 (1992) 1413–1449.
- [14] F. Brezzi, K.J. Bathe, A discourse on the stability conditions for mixed finite element formulations, *Comput. Methods Appl. Mech. Eng.* 82 (1990) 27–57.